



Cite this: *Phys. Chem. Chem. Phys.*,
2017, 19, 4725

Pressure-induced silica quartz amorphization studied by iterative stochastic surface walking reaction sampling†

Xiao-Jie Zhang, Cheng Shang and Zhi-Pan Liu*

The crystal to amorphous transformation is a common phenomenon in Nature and has important impacts on material properties. Our current knowledge on such complex solid transformation processes is, however, limited because of their slow kinetics and the lack of long-range ordering in amorphous structures. To reveal the kinetics in the amorphization of solids, this work, by developing iterative reaction sampling based on the stochastic surface walking global optimization method, investigates the well-known crystal to amorphous transformation of silica (SiO₂) under external pressures, the mechanism of which has long been debated for its non-equilibrium, pressure-sensitive kinetics and complex product components. Here we report for the first time the global potential energy surface (PES) and the lowest energy pathways for α -quartz amorphization from first principles. We show that the pressurization at 15 GPa, the reaction condition, can lift the quartz phase energetically close to the amorphous zone, which thermodynamically initializes the amorphization. More importantly, the large flexibility of Si cation coordination (including four, five and six coordination) results in many kinetically competing routes to more stable dense forms, including the known MI, stishovite, newly-identified MII and TI phases. All these pathways have high barriers due to the local Si–O bond breaking and are mediated by amorphous structures with five-fold Si. This causes simultaneous crystal-to-crystal and crystal-to-amorphous transitions. The high barrier and the reconstructive nature of the phase transition are the key kinetics origin for silica amorphization under pressures.

Received 8th October 2016,
Accepted 9th January 2017

DOI: 10.1039/c6cp06895b

rsc.li/pccp

1. Introduction

Amorphization and crystallization of materials are common phenomena in Nature with important applications, *e.g.* in phase-change materials.^{1,2} The amorphization of solids can be achieved by different synthetic approaches, *e.g.* by heating, pressurization or chemical doping. Silica (SiO₂) with flexible Si coordination possesses many polymorphs under ambient conditions and is well known for the crystal-to-amorphous (glass) transformation at elevated temperatures. On the other hand, the pressure-induced amorphization (PIA) of silica, which also destroys the long-range ordering, is much poorly understood for its non-equilibrium pressure-sensitive kinetics.^{3,4} Because of

its important roles in Nature, the PIA of α -quartz (Q, *P*_{3,21}, #154) was extensively studied in the past 30 years.^{5–7} The reaction exhibits complex pressure-dependent kinetics, where both crystal-to-crystal and crystal-to-amorphous transformations appear to occur simultaneously. Despite it sharing similar amorphous structural features with densified silica glass *via* melt-quenching,⁷ the PIA product has its own intriguing properties that remain poorly understood microscopically, including anomalous elastic kinetics,⁸ and fast recrystallization and mixing with many crystalline phases.⁹

To date, only three post-quartz crystalline phases have been assigned from experiment during PIA of silica at ambient temperature, including quartz II (QII, *C*₂, #5), the monoclinic MI phase (*P*_{2,1/c}, #14) and stishovite (St, *P*_{4,2/mnm}, #136). Among them, QII forms first in the pressure range of 15 to 25 GPa, whereas the MI phase starts to evolve above 21 GPa, and persists even at 40 GPa. Although the stishovite phase, containing only six-coordinated [SiO₆] octahedra, is the thermodynamically most stable phase above 9 GPa,¹⁰ it appears very late in PIA and can be assigned clearly only above 60 GPa.¹¹ Importantly, the amorphization accompanies throughout the evolution of crystalline phases as evidenced by the salient amorphous structural features

Collaborative Innovation Center of Chemistry for Energy Material, Key Laboratory of Computational Physical Science (Ministry of Education), Shanghai Key Laboratory of Molecular Catalysis and Innovative Materials, Department of Chemistry, Fudan University, Shanghai 200433, China. E-mail: zpliu@fudan.edu.cn

† Electronic supplementary information (ESI) available: Other details on methods and calculation setups; enthalpy difference between quartz and stishovite at different pressures; phase transition pathways from QII to stishovite and MII; simulated XRD patterns; the atomic XYZ positions for all the states along the pathway. See DOI: 10.1039/c6cp06895b

due to the formation of undercoordinated $[\text{SiO}_{4/5}]$.¹² These observations indicate that PIA is kinetically controlled and far from thermodynamic equilibrium. The PIA products below 40 GPa might be a mixture of quartz, QII and MI crystalline phases together with unknown amorphous components.⁹

While the amorphization/crystallization phenomena are often interpreted conceptually using the underlying potential energy surface (PES) of materials where kinetic barriers are present to separate crystalline and amorphous phases, the PES construction and the pathway search have been formidable tasks in theory. As to PIA, the presence of multiple channels in various products including the amorphous phase and the extremely slow kinetics of solid transformation are two major obstacles for simulations to observe the process. The former implies that finding the lowest energy pathway is technically challenging due to the large density of states in the amorphous zone. For the slow kinetics, modern theoretical techniques are frustrated by too limited simulation timescale to overcome high barriers in solid reactions.^{13,14} Until recently, Martoňák *et al.*¹⁵ using lattice-driven metadynamics with the classical potential discovered a sequential $\text{Q} \rightarrow \text{QII} \rightarrow \text{MI} \rightarrow \text{stishovite}$ crystal-to-crystal pathway for silica at 15 GPa. As a result, many fundamental questions remain open, such as why stishovite is highly kinetically hindered and why the amorphous phase is produced simultaneously. This asks for quantitative kinetics data to distinguish different reaction channels at the quantum mechanics level of accuracy, which are, however, practically infeasible to obtain using traditional techniques.

In this work, we have utilized the recently developed stochastic surface walking (SSW) method to explore the global PES of SiO_2 and outline the key structural and energetic criteria to distinguish the SiO_2 amorphous from crystalline phases. To map out the complex solid-to-solid phase transition reaction network from α -quartz to other crystalline phases, we develop an iterative reaction sampling technique based on the SSW reaction sampling method. We demonstrate that upon pressurization α -quartz first arrives in the QII phase and the phase transition starts to bifurcate into several kinetically competing routes leading to MI, St and other dense phases, all mediated by amorphous structure intermediates. This complex reaction network clarifies the physical origin of PIA at the atomic level.

2. Methods and calculation details

a. PES exploration

The SSW algorithm¹⁶ implements an automated climbing mechanism to manipulate a structural configuration from a local minimum to a high-energy configuration along one random mode direction. The method was initially developed for aperiodic systems, such as molecules and clusters,¹⁷ and has been extended to periodic crystals.¹⁸ A brief introduction of the SSW algorithm is also given in the ESI,† Section IA.

The SSW method in combination with the Wang–Landau algorithm (SSW-WL)^{19,20} was first utilized to explore the PES of the SiO_2 phase space, which takes advantage of the global

optimization from the SSW method (see our previous work for a detailed methodology of SSW^{16,18,21}) and the density of states (DOS, $g(H)$) computation from the WL method. The WL algorithm is a Monte Carlo method designed to calculate the density of states of a system. It uses a non-Markovian stochastic process which asymptotically converges to a multicanonical ensemble. In this work, the DOS $g(H)$ is a function of the enthalpy H of minima, *i.e.* the number of local minima within the interval $(H, H + dH)$. SSW-WL can resolve the DOS, $g(H)$, of minima *via* performing a set of random walks in the enthalpy space with a probability proportional to the reciprocal of $g(H)$, where the SSW method acts as the engine of random walks on the PES.²⁰

In all calculations, the enthalpy of a structure (H) can be derived following the standard thermodynamics, $H = U + PV$, where U is taken as the total energy E of the structure from calculations as the thermal contribution can be neglected for solid phases at low temperatures, P is the external pressure and V is the volume of the lattice. The hydrostatic external pressure is applied by using the equation $\sigma_{\text{tot}} = \sigma_{\text{latt}} - PI$, where σ_{tot} is the total stress, σ_{latt} is the lattice stress tensor and I is a unit matrix.²²

b. Reaction sampling

We have recently developed a new reaction sampling method based on SSW global optimization, namely SSW reaction sampling (SSW-RS).²³ The SSW-RS combines SSW PES exploration and the double-ended surface walking (DESW) method²⁴ of transition state (TS) location for finding the lowest energy pathway of relatively simple reactions (*e.g.* one-step reaction), *i.e.* $\text{min}(\text{A} \rightarrow \text{B})$ between A and B, the predefined reactant/product phases. To do so, all possible connections in between A and B are sampled using SSW-RS from which the lowest energy pathway is identified by sorting the computed barriers. The SSW-RS was applied previously in ZrO_2 and TiO_2 solid phase transitions.^{25,26}

The SSW-RS is fully automated and divided into three stages in simulation, namely, (i) pathway collection *via* extensive SSW global search; (ii) pathway screening *via* fast DESW pathway building;²⁴ and (iii) lowest energy pathway determination *via* DESW TS search. The first stage is the most important and most time-consuming part, which generates all the likely pairs of generalized reaction coordinates linking different crystal phases. More details on the SSW-RS are provided in the ESI† and also in our previous works.²³

As this work is concerned about the amorphization pathways where a significant number of minima are present in the amorphous zone, the reaction pathways are complex and naturally contain multiple steps. For multiple-step reactions (*i.e.* with multiple TSs) with multiple reaction channels, *e.g.* $\text{A} \rightarrow \text{B}$ with i and j being possible intervening minima, we note that the reaction pathway can be similarly solved by separating the pathway into pair-wise linkages, *i.e.* $\text{A} \rightarrow i$, $i \rightarrow j$ and $j \rightarrow \text{B}$, if the intervening minima are known in advance. Each lowest energy pathway, $\text{min}(\text{A} \rightarrow i)$, $\text{min}(i \rightarrow j)$ and $\text{min}(j \rightarrow \text{B})$, can be revealed using SSW-RS by sampling intervening i and j states. It is therefore critical to identify intervening minima that are present in the lowest energy pathway, which should now be solved iteratively.

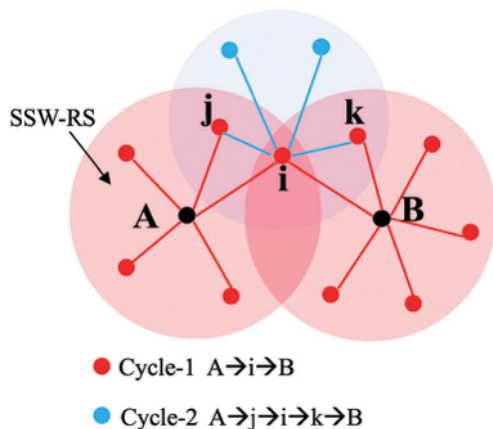


Fig. 1 Scheme showing the iterative SSW-RS simulation to resolve a complex reaction network in between A and B minima where the lowest energy pathway has multiple reaction steps. Each circle represents an independent SSW-RS to identify the pathways starting from the central minima. Different pathways connecting A and B with i , j and k being intervening minima are obtained from two iteration cycles, from which the lowest energy pathway can be determined and updated.

In this work, we developed an iterative SSW-RS for evolving complex reaction networks. A simple scheme of the iterative SSW-RS is shown in Fig. 1 and is explained as follows. In each cycle of iteration, the new intervening minima that can connect A to B will be sampled using SSW-RS, from which a number of low energy pathways are determined and collected according to the two-state rate theory.²⁷ From these low energy pathways, the intervening minima that have not been sampled previously are identified and fed as input for the next cycle. The initial intervening minima (at cycle 1) can be quite arbitrary as long as they form linkages from A to B. In this work, they are taken from the minima reachable from both A and B in SSW-RS, *i.e.* $A \rightarrow i$, $B \rightarrow i$ (see Fig. 1), since A and B are not very far on the PES for SiO₂ minima. During iteration, the connectivity between adjacent minima on the PES will be established and updated using their lowest energy pathway.

c. Calculation details and DFT setups

Because SSW-WL sampling and SSW-RS calculations detailed above require that a significant number of data on the PES (*i.e.* at least 10^6 minima) be sampled, the classical van Beest, Kramer, and van Santen (BKS) potential²⁸ was first adopted in these SSW-based calculations to retrieve the structure and enthalpy of phases. The BKS potential has been demonstrated to yield a good structure and reasonable energetics for the SiO₂ system.^{15,29} After testing 12-, 18-, 24- and 36-atom supercells, our SSW-WL simulation utilizes 36-atom supercells to obtain the global PES for SiO₂ phases, which turns out to be large enough to reveal all the concerned crystalline phases and to yield a large density of states for amorphous structures. Our SSW-RS simulation utilizes the 18-atom supercell to describe the solid phase transition from quartz to quartz-II and to other high pressure crystalline phases. In order to obtain more accurate energetics, the structures obtained using the BKS potential are further refined

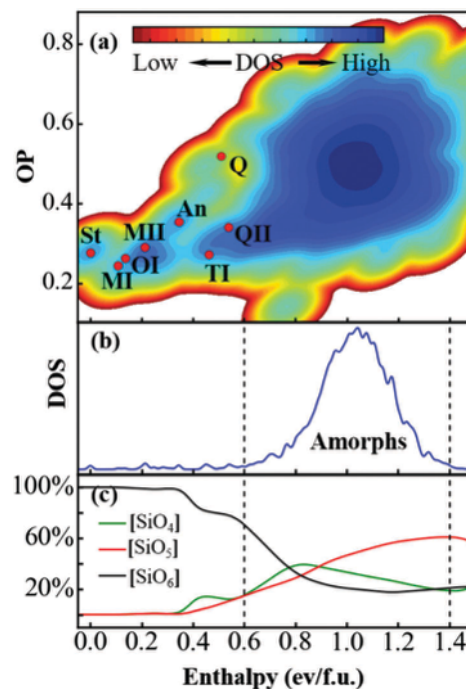


Fig. 2 (a) PES contour plot for SiO₂ phases at 15 GPa from SSW-WL minimum sampling. The x-axis is the enthalpy (eV f.u.⁻¹) of the phases and the y-axis is the distance-weighted Steinhardt-type order parameter ($l = 2$) in eqn (2). The enthalpy of stishovite (global minimum) is set at zero. Important crystalline phases are indicated by red spots, including stishovite (St), monoclinic I (MI), the α -PbO₂ structure (OI), monoclinic II (MII), the anatase structure (An), triclinic I (TI), quartz-II (QII) and α -quartz (Q). (b) Wang-Landau DOS for SiO₂ phases, showing that amorphous structures are in the 0.6–1.4 eV f.u.⁻¹ window. (c) The percentage of differently coordinated Si averaged for SiO₂ phases. Undercoordinated Si ([SiO₄] and [SiO₅]) are main structural features for amorphous structures.

using plane-wave DFT calculations, *i.e.* a 36-atom supercell for the PES (as shown in Fig. 2) and an 18-atom supercell for the reaction pathway (as shown in Fig. 3). Specifically, $\sim 10\,000$ minima on the PES with an appreciable $g(H)$ and the lowest 20 reaction pathways starting from quartz to other polymorphs are refined using plane-wave DFT calculations.

We have compared the DFT and BKS data for enthalpy change from quartz to stishovite with the available experimental data in the ESI,[†] Table S1, from 0 GPa to 30 GPa. While the structures obtained from both DFT and BKS are consistent (see the ESI,[†] Table S2), DFT can reproduce the pressure dependence of enthalpy and the absolute error at 15 GPa is less than 0.06 eV f.u.⁻¹, but BKS fails, not surprisingly, to correctly describe the enthalpy trend and the absolute value is qualitatively wrong at 0 GPa. It was previously noticed that BKS tends to overestimate the stability of dense forms.³⁰ In this work, we are interested in the global PES of silica at 15 GPa, where BKS predicts correctly stishovite being more stable than quartz. Therefore, the BKS is mainly utilized as a tool to collect structures on the global PES (note that the parameterization of an empirical potential that fits all crystalline phases on a global PES is technically very challenging and is not available in general). To illustrate the good structure from BKS, we have compared

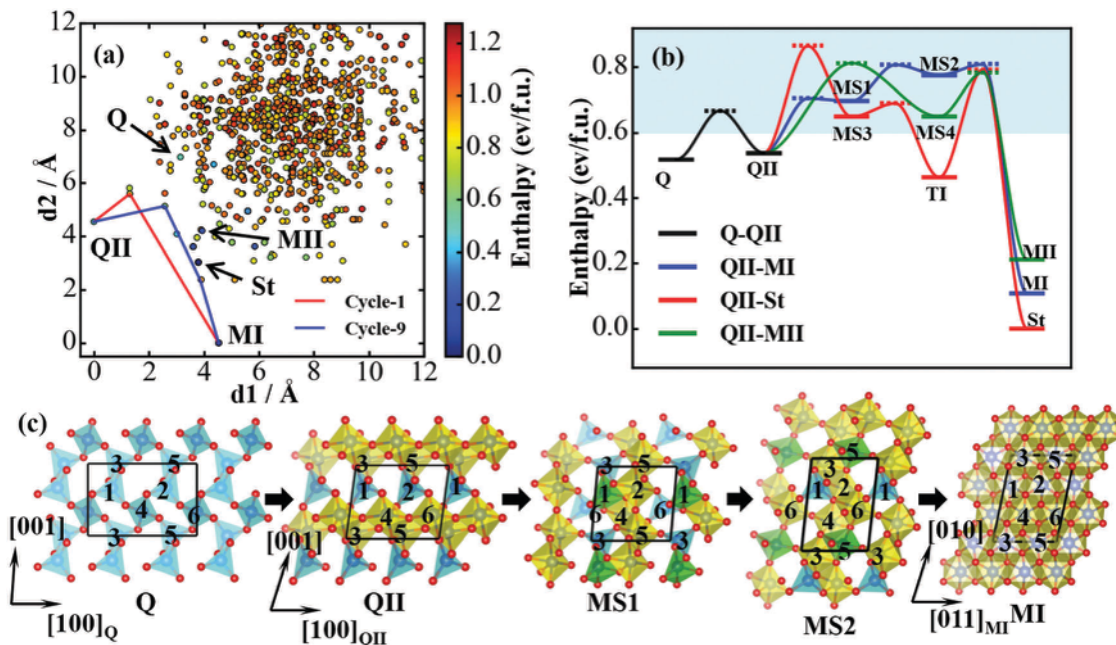


Fig. 3 (a) Distance–distance map for SiO_2 phases generated from iterative SSW-RS. The x-axis and y-axis are the distances of a SiO_2 phase from QII (d1) and from MI phases (d2) in an 18-atom supercell, respectively (also see the ESI†). The QII-to-MI lowest energy pathways after cycle-1 and cycle-9 (converged) during iterative SSW-RS are indicated on the map. (b) Reaction profile from Q to QII, MI, stishovite (St) and MII phases showing the lowest energy pathway as determined from iterative SSW-RS. Solid/dashed lines represent minima/TSS along the pathways. The colored area indicates the amorphous zone. (c) Reaction snapshots along the pathway from Q to MI, showing the reconstructive nature of the solid phase transition. Polyhedron representation is used for all structures: yellow: $[\text{SiO}_6]$, green: $[\text{SiO}_5]$, light blue: $[\text{SiO}_4]$.

the reaction pathway (see Fig. 3) from quartz to MI using DFT and BKS in the ESI,† Fig. S1. The optimized structures including the intermediates along the pathway from BKS are very similar to those from DFT (error $< 2\%$ for lattice parameters and $< 3\%$ for Si–O bond lengths), although the energetics from BKS are up to ~ 0.2 eV f.u. $^{-1}$ higher.

All DFT calculations without specifically mentioning were carried out using a plane-wave program as implemented in the Vienna ab initio simulation package (VASP).^{31,32} The kinetic energy cutoff utilized was 500 eV and the ionic core electrons were described using the projector augmented wave (PAW) pseudo-potential.³³ The exchange–correlation functional utilized was the GGA-PBE functional.³⁴ The k -point mesh in the first Brillouin zone was sampled using the Monkhorst–Pack scheme³⁵ with a $(4 \times 4 \times 4)$ grid. For all the structures, both lattice and atomic positions were fully optimized until the maximal stress component is below 0.01 GPa and the maximal force component is below 0.01 eV \AA^{-1} .

To examine the dynamic behaviour of amorphous structures, finite-temperature molecular dynamics (MD) calculations were carried out in the framework of first principles DFT as implemented in the SIESTA package³⁶ with numerical atomic orbital basis sets³⁷ and Troullier Martins norm-conserving pseudo-potentials.³⁸ The exchange–correlation functional utilized was GGA-PBE.³⁴ The optimized double- ζ plus polarization (DZP) basis sets were employed for all elements to expand the molecular orbitals. The energy cutoff for the real space grid used to represent the density was set as 150 Ry. The constant-temperature and

constant-pressure MD simulations utilizes the Nosé–Hoover thermostat^{39,40} and the Parrinello–Rahman barostat,⁴¹ *i.e.* the NPT ensemble to maintain 300 K and 15 GPa. The time step in MD was set at 1 fs.

It should be mentioned that the PIA experiment is carried out at ambient temperature (~ 300 K), where the entropy contribution to free energy is small. Experimentally, for quartz–stishovite phase transition, the entropy contribution to the free energy difference between the two phases at 300 K is around -0.05 eV f.u. $^{-1}$.⁴² This is consistent with our own calculations based on phonon density corrections to the free energy (< -0.05 eV f.u. $^{-1}$) and also with the previous calculations.⁴³ In this work, we utilize the enthalpy term to compare the phase stability and the kinetics between different phase transition pathways.

3. Results and discussion

a. Global PES

Our investigation starts by exploring SiO_2 minima on the PES under pressure, which has two objectives: (i) to reveal all important crystalline phases and (ii) to identify the amorphous zone on the PES that ought to have a large density of states (DOS). The technique we utilized is a recently-developed SSW-WL method, as detailed in Section 2. More than 10^7 minima were visited and 8 WL cycles were taken to eventually reach the flat histogram in WL DOS.

The minima on the PES can be distinguished by using a distance-weighted Steinhardt-type order parameter (OP).

The original Steinhardt OP⁴⁴ considers only the first shell bonds and is defined as follows (eqn (1)):

$$OP_l = \left(\frac{4\pi}{2l+1} \sum_{m=-l}^l \overline{|Y_{lm}(\mathbf{n})|^2} \right)^{1/2} \quad (1)$$

where Y_{lm} is the spherical harmonic function of degree l and order m ; \mathbf{n} is the normalized direction between all bonded atoms, and the bar over Y_{lm} means the average over all bonded atoms. To better distinguish the states on the PES, here we design a distance-weighted OP (eqn (2)):

$$OP_l = \left(\frac{4\pi}{2l+1} \sum_{m=-l}^l \left| \frac{1}{N_{\text{bonds}}} \sum_{i \neq j} e^{-\frac{r_{ij}-r_c}{2}} Y_{lm}(\mathbf{n}) \right|^2 \right)^{1/2} \quad (2)$$

where i and j are atoms in the lattice, r_{ij} is the distance between atom i and j , and r_c is set at 60% of the typical single bond length for i and j atoms (e.g. ~ 1.8 Å for a Si-O bond and r_c is 1.08 Å). N_{bonds} is the number of bonds (in the first bonding shell). By choosing a suitable degree l , the order parameter can measure the short- and medium-range ordering of atoms in the lattice. For structures with high symmetries, e.g. most of the crystalline phases in Fig. 2 (degree $l = 2$), the terms in the equation tend to cancel largely and the overall OP is small.

We then utilize DFT calculations to re-optimize the distinct minima with the DOS $g(H) > 10^{-4}$ (more than 10 000 minima). The PES of SiO₂ phases under 15 GPa with DFT energetics is thus obtained, as shown in the enthalpy-OP contour plot in Fig. 2a and the DOS of minima is projected in Fig. 2b. The coordination environments of Si for all structures are analyzed and plotted in Fig. 2c. The energetics (H) and the structural information for the key structures are listed in Table 1.

Fig. 2a shows that all the common phases of SiO₂ together with many new phases are identified from SSW-WL PES sampling. As expected, the lowest energy phase is stishovite, which is defined as enthalpy zero in the figure. The next three stable structures are MI, OI (α -PbO₂ like phase, Pbcn, #60) and MII ($C2/m$, #12, a monoclinic structure not reported previously), which are 0.2–0.3 eV per formula unit (f.u.) less stable than stishovite.

Table 1 SiO₂ polymorphs during PIA.^a All data correspond to 15 GPa

| Silica phase | Space group | Volume (Å ³ f.u. ⁻¹) | H (eV f.u. ⁻¹) | SiO _x ^b (x = 4/5/6) % |
|--------------|-------------|---|----------------------------|---|
| Q | $P3_221$ | 31.21 | 0.51 | 100/0/0 |
| QII | $C2$ | 24.85 | 0.54 | 33/0/67 |
| MI | $P2_1/c$ | 22.69 | 0.11 | 0/0/100 |
| St | $P4_2/mnm$ | 22.95 | 0.00 | 0/0/100 |
| MI | $C2/m$ | 23.82 | 0.21 | 0/0/100 |
| MS1 | $P1$ | 25.51 | 0.70 | 33/16/51 |
| MS2 | $P1$ | 25.93 | 0.78 | 50/16/34 |
| MS3 | $P1$ | 23.43 | 0.65 | 0/33/67 |
| TI | $P1$ | 23.21 | 0.46 | 0/0/100 |
| MS4 | $P1$ | 26.89 | 0.65 | 67/0/33 |

^a Listed silica phases include crystalline phases quartz (Q), quartz-II (QII), stishovite (St), monoclinic I (MI), monoclinic II (MI), triclinic I (TI) and amorphous structures (MS1-4) along the reaction pathway shown in Fig. 3. ^b The percentages for four, five and six coordinated Si cations in the silica phase.

Quartz and QII phases are not stable at 15 GPa, being more than 0.4 eV f.u.⁻¹ above stishovite. Many other crystalline phases can also be observed on the PES, such as anatase, but they are situated in a higher energy region, from 0.2 to 0.4 eV f.u.⁻¹ The Cartesian structures of these crystalline phases are detailed in the ESI.†

Moving away from the low energy crystalline phases, one can see readily a salient deep-blue zone in the figure, which spans from 0.60 to 1.40 eV f.u.⁻¹, featuring a high, continuous and broad peak in the DOS plot (Fig. 2b). There are many energy-degenerate structures in this high energy window, implying that the amorphous structures dominate this area and they have much larger configuration entropies than the crystal structures.

The coordination of Si is an important geometrical feature, commonly utilized to distinguish the crystalline from the amorphous phase. As shown in Fig. 2c, the concentrations of [SiO₄], [SiO₅] and [SiO₆] for the phases vary continuously with the increase of enthalpy. For the low energy phases (e.g. stishovite, MI, OI and MII), they generally have only SiO₆ octahedra (100% [SiO₆], Table 1). This is consistent with the high-pressure conditions that favor dense crystalline forms. [SiO₄] and [SiO₅] start to appear for the structures above 0.33 eV f.u.⁻¹ and become the key structural feature for amorphous structures: they account for up to 80% Si in the region. We noted that quartz, although being the most stable crystalline phase at ambient pressure, is located now close to the amorphous zone at 15 GPa (Fig. 2a), apparently because it contains only SiO₄ and is much destabilized at high pressures. Similarly, QII, as another major phase during the PIA of SiO₂, is located at the low energy tail of the amorphous zone with 2/3 SiO₆ and 1/3 SiO₄ (Table 1).

To be specific, we define the SiO₂ amorphous phase as a broad area on the global PES with a large DOS, $g(H) > 3 \times 10^{-4}$, where (i) the enthalpy spectrum becomes continuous due to the energy degeneracy, (ii) the structure spectrum as measured by the order parameter becomes also continuous, and (iii) the local structures differ markedly from all crystalline phases with appreciable concentrations of 4- and 5-coordinated Si cations. This leads us to quantify the energetics of amorphous structures as ~ 0.6 eV f.u.⁻¹ above the most stable stishovite crystal phase, as indicated by the dotted line in Fig. 2b and c.

b. Reaction pathways

With all important minima identified, our next task is to locate the lowest energy pathways connecting them, which can be used to deduce kinetics between phases. The iterative SSW-RS as schematically shown in Fig. 1 can find the lowest energy pathway between a pair of SiO₂ phases typically within 10 cycles, where more than 100 intervening minima are sampled until the lowest energy pathway converges. For the high computational load, all pathway searches were carried out using the BKS potential in an 18-atom supercell and were further verified in a 36-atom supercell to ensure the located lowest energy pathway. Considering that the classical potential is not accurate enough, we have utilized plane-wave DFT calculations to re-optimize at least 20 lowest energy pathways obtained from the iterative SSW-RS, each with a distinct rate-determining step. In DFT refinement,

the minima and TSs are fully optimized until all the forces and stresses diminish. We note that DFT calculations are essential for identifying the lowest energy pathway, which is generally not the lowest in force field results. Using the approach, we have searched the reaction pathways starting from α -quartz to other dense phases, including QII, MI, MII and stishovite phases.

To illustrate how such a solid phase transition pathway is identified, we take the QII-to-MI pathway as an example. Fig. 3a shows the pathway evolution by plotting the shortest Euclidean distances (d) of phases to QII and to MI phases. For phase i , for example, d of $i \rightarrow$ QII is the length of the shortest path from i to QII by summing all intervening linkages, where the distance for each pair of linkages is directly available from SSW-RS (also see the ESI†). As shown in Fig. 3a, QII and MI are located at coordinates (4.54, 0) and (0, 4.54), respectively, and most phases are far away from them with distances more than 6.0 Å. The lowest energy pathway tends to be short pathways linking two phases in general. The lowest energy pathway after cycle 1 (red lines) is a two-step reaction with an overall barrier of more than 0.35 eV f.u.⁻¹ with respect to QII. The intermediate is located at coordinate (1.31, 5.59) in the figure. The overall barrier then decreases gradually during iteration as more and more minima on the PES are sampled. The lowest energy pathway converges to 0.27 eV f.u.⁻¹, which is the overall barrier after nine cycles (blue lines). The final pathway has two intermediate phases, namely MS1 and MS2, located at coordinates (2.58, 5.13) and (3.87, 2.36) in Fig. 3a, which are geometrically close to QII and MI, but are much higher in energy (0.70 and 0.78 eV f.u.⁻¹ above the stishovite phase for MS1 and MS2, respectively, also discussed below).

All important lowest energy pathways starting from quartz are summarized in Fig. 3b, which end with different dense phases, *i.e.* QII, MI, MII and stishovite. Importantly, we found that the Q-to-QII transition is a one-step reaction with a low barrier, but the pathways from QII to other phases are kinetically competing. There are two intermediate phases from QII to stishovite, namely MS3 and TI (triclinic, P1), and one intermediate phase from QII to MII, namely MS4 (also see the ESI† for structural data). The overall barrier follows the order QII (0.15) \ll MI (0.29) $<$ MII (0.30) $<$ stishovite (0.34 eV f.u.⁻¹) at 15 GPa, implying that QII is always first produced and MI is preferred slightly over other dense forms. These kinetic data confirm the observations on the preference of QII and MI phases below 25 GPa in PIA.⁹

Using the DFT barrier of phase transitions, we may further estimate the rate for Q-QII and QII-MS1 (amorphization) phase transitions under 15 GPa. In order to form the smallest structural unit, *i.e.* 6 SiO₂ f.u., the rate constant for Q-QII phase transition is $4.74 \times 10^{-3} \text{ s}^{-1}$, while that for QII-MS1 is $3.95 \times 10^{-5} \text{ s}^{-1}$ at room temperature. This suggests that the timescale to observe a 10 nm size new phase (crystal size estimated from XRD graphs using Scherrer's equation⁴⁵) would be 50 minutes for the QII phase but 100 hours for amorphization. This matches with the timescale in the PIA experiment, *e.g.* 24 h pressurization,⁹ where various defects are present to expedite the phase transition.

As a representative, we here describe in detail the mechanism for the Q to MI transition based on the lowest energy pathway at 15 GPa. The pathways to the other dense phases are shown in the ESI.† The snapshots for the Q-to-MI pathway are displayed in Fig. 3c, which can be divided into two stages. For the first stage, the Q-to-QII transition, we note that the phase transition involves a large volume drop by 20.3% (from 31.21 to 24.85 Å³ f.u.⁻¹) with a maximal principal compression along the [100] direction (a axis from 9.11 to 6.91 Å). The lattice also experiences a large distortion with the α angle changing from 90° to 72°. The Q-to-QII transition belongs to the reconstructive phase transition. In accordance with the large volume decrease, two thirds of Si atoms (3–6 polyhedra in Fig. 3c) increase coordination from 4-fold to 6-fold by edge sharing.

For the second stage, the QII-to-MI transition, the volume (see Table 1) experiences an initial increase, quite unexpectedly, due to the presence of MS1 (25.51 Å³ f.u.⁻¹) and MS2 (25.93 Å³ f.u.⁻¹) followed by the reduction when MI (22.69 Å³ f.u.⁻¹) is reached. The highest energy TS occurs at the step from MS2 to MI, which dictates the overall barrier height (0.29 eV f.u.⁻¹ with respect to Q). The overall maximal principal compression occurs along the [010] direction of QII (b axis from 4.62 Å to 4.05 Å). The atomic motion is mainly along the [111] of QII with a maximal traveling distance of 2.21 Å per atom. The large volume change together with short-range atomic motion indicates that the phase transition is also a reconstructive phase transition. Specifically, from QII to MS1, tetrahedron 2 (labelled in Fig. 3c) moves close to octahedron 3, and tetrahedron 1 attaches to octahedron 4. From MS1 to MS2, tetrahedra 3 and 6 join with octahedron 2, forming one compact [SiO₆] layer (3, 2 and 6). From MS2 to MI, polyhedra 1, 4 and 5 move close to each other, forming another compact [SiO₆] layer.

It should be mentioned that for all the silica solid phase transitions in Fig. 3, we did not observe any atomic layer shearing in the lowest energy pathway, which is otherwise an important feature for many diffusionless solid phase transitions, such as those in TiO₂ and ZrO₂^{25,26} and the pressure-induced transformation of Zr(Ti).⁴⁶ The atomic layer shearing movement is typical in Martensitic diffusionless transition, the presence of which would indicate the formation of coherent interfaces during the new phase growth and a relatively low barrier of solid phase transition. On the other hand, the lack of a shearing plane in silica transformation suggests that the phase transition is not Martensitic but dominated by the local Si polyhedron movement (as illustrated clearly in Fig. 3 from Q to MI). Due to the difficulty in maintaining coherent interfaces between nascent nuclei and the host, such reconstructive phase transitions involve local Si-O bond breaking and need to surmount a high barrier in order to produce a new phase.

In line with the reconstructive transition mechanism, our results reveal that the presence of high-energy amorphous intermediates is an important and common feature in the transition from quartz to MI, MII and stishovite phases, including MS1 and MS2 in the Q-to-MI pathway, MS3 in QII-to-St and MS4 in QII-to-MII. As also listed in Table 1, these phases are all in low P1 symmetry, contain five-fold Si [SiO₅], have a larger volume

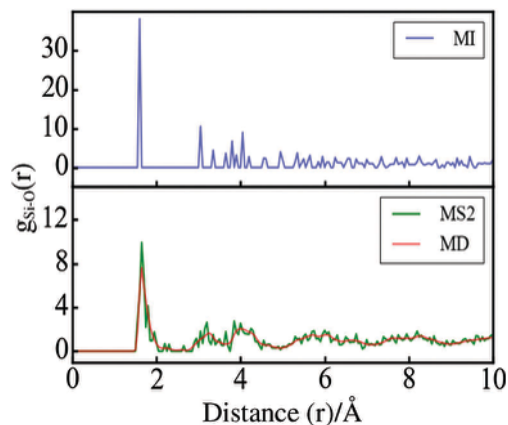


Fig. 4 Radial distribution function for the Si–O distance ($g_{\text{Si-O}}(r)$) for MI, MS2 (initial structure in MD) and the equilibrated MS2 after 10 ps first-principles MD simulation.

than their dense products and lack sharp peaks in the Si–O radial distribution function (RDF) plot (see Fig. 4), exhibiting salient amorphous characteristics. Because of the slow kinetics in solid transition and the large DOS in the amorphous zone, the amorphous intermediates appearing in the pathways support strongly that the crystal-to-crystal transition must be accompanied by the crystal-to-amorphous reactions in PIA.

Considering that MS2 in the MI formation pathway is a representative amorphous structure, we have examined the dynamics of this amorphous structure using first principles MD simulation (see Calculation details in section 2c). In our simulation, the system contains 144 atoms (48 f.u.) in total with the initial structure taken from the MS2 state by increasing the 36-atom cell to the $(2 \times 2 \times 1)$ supercell. The system was kept in the 300 K thermostat and the 15 GPa barostat (NPT ensemble), and ran 5 ps for equilibration and another 5 ps for trajectory collection. In the 10 ps simulation, no phase transition was found as expected (as also evident from the RDF), as the PIA solid reactions are very slow at ambient temperature.

The RDF for the Si–O distance of the equilibrated MS2 from the MD trajectory is shown in Fig. 4 (red line), which is compared with those from the crystalline MI phase (blue line) and the initial structure of MS2 (green line). It can be seen that both the initial MS2 structure and the equilibrated MS2 are very different from the crystalline MI, where a very sharp first neighbor peak (belonging to SiO_6 octahedra) appears together with discrete peaks from 3 to 6 Å, which are second and third neighbor Si–O interactions. The initial MS2 structure has a much lower first Si–O peak compared to that in MI, in agreement with the appearance of SiO_4 and SiO_5 in MS2 (Table 1). The finite-temperature MD further smoothens the continuous peaks of the initial MS2 structure, leading to an even lower first-neighbor peak and very broad continuous peaks tailing to 10 Å. Such an RDF is typical of amorphous/glass states⁴⁷ and thus it confirms the production of amorphous structures during the quartz to MI transformation.

We also compared the amorphous structures from MD simulation (MS2) with that reported by Ugliengo *et al.*,⁴⁸ who optimized an amorphous glass structure using the B3LYP

hybrid functional. Their amorphous structure was obtained from MD simulation at 6000 K followed by cooling down to 300 K. For our amorphous structure at zero pressure, the average of the Si–O bond length is 1.667 Å, which is slightly greater than 1.658 Å in the reference; the average O–Si–O angle is 108.9°, slightly smaller than that in the reference (109.3°). The good structural agreement also validates the amorphous structure model from this work.

With the determined pathways at 15 GPa, we are able to extrapolate the kinetics of PIA to other pressures. These pathways (Fig. 5) are re-optimized at 10, 20, 25 and 30 GPa, and the overall barrier for each is determined and plotted in Fig. 5. As discovered from Fig. 5, the barrier of the Q-to-QII transition is not high in general and diminishes at 30 GPa. In fact, the barrier is much lower than those to the other phase transitions and is very sensitive to the external pressure. This can be attributed simply to thermodynamics: QII becomes more stable at high pressures due to its much smaller volume than quartz (by 20%). The Q–QII phase transition is thus reversible as controlled by pressure. This explains the anomalous elastic kinetics upon the change in pressure in experiment.⁷

By contrast, the overall barriers to the dense phases, including MI, MII and stishovite, remain high (> 0.3 eV f.u.^{−1}) even at high pressures. Below 15 GPa, the rapid destabilization of quartz helps reduce the barrier; above 15 GPa, QII becomes more stable than quartz and the overall barriers to MI and MII increase instead since the reaction from QII to amorphous intermediates now dominates the barrier, which needs to expand the volume that works against the pressure increase. Our results indicate that the selectivity towards MI does not benefit significantly by elevating pressure.

The TI phase in the QII-to-S pathway is worthy of special attention, which is a dense phase with only six-fold Si. The transition from the TI to stishovite phase is kinetically hindered by a high barrier (0.33 eV f.u.^{−1} at 15 GPa), which is rather constant upon the change in pressure. Considering that the barrier of the QII-to-TI transition is 0.35 eV f.u.^{−1} at 15 GPa and continues to drop with the increase of pressure (Fig. 5), the TI-to-stishovite reaction becomes the rate-determining step for stishovite formation after 15 GPa. The barrier to TI intersects

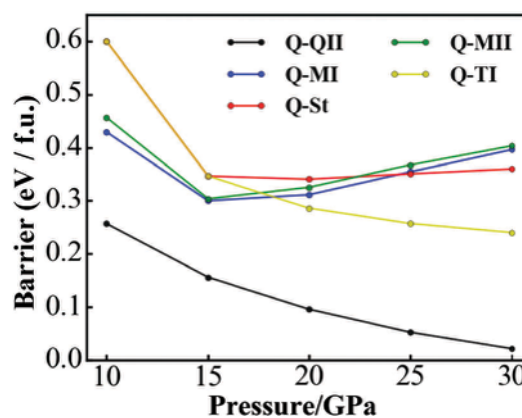


Fig. 5 Reaction overall barriers from quartz to different phases at various pressures.

with that to MI at 18.2 GPa (Fig. 5), implying that the TI phase is also a kinetically allowed product in PIA. The dense TI phase acts as a kinetic trap in the pathway to stishovite, leading to the great difficulty in yielding the stishovite phase even at high pressures.

The observed “fast recrystallization” in PIA⁶ can therefore be explained by the incomplete solid phase transition from QII to the other dense forms, apparently due to the high barrier of these reconstructive phase transitions. The solid phase transitions from QII to the other dense forms are trapped in the intermediate amorphous structures. When the high pressure is released, the crystalline structure could be recovered rapidly.

4. Conclusions

By constructing the global PES and developing an iterative pathway sampling method, this work resolves the physical origin for the pressure-induced amorphization of SiO₂. While the destabilization of the initial state (quartz) by high pressures provides the thermodynamic force driving the solid phase transition, we find that the presence of intervening amorphous structures in multiple crystal-to-crystal pathways is the key to this non-equilibrium amorphization phenomenon. The lowest energy pathways for the SiO₂ crystal-to-crystal solid phase transition determined from this work not only deepen our understanding in general for the complex crystal-to-amorphous solid phase transition, but also pave the way towards the rational design of phase-change materials based on the modern global optimization and pathway sampling methods. The main results of this work are outlined below.

(i) Quartz is first converted to Quartz-II upon pressurization. The reaction is driven by thermodynamics and thus sensitive to pressure because of the large volume difference between the two phases.

(ii) QII can further transform into a number of dense phases, including MI, MII, TI and stishovite, which are, however, not sensitive to the external pressure above 15 GPa. While these reactions are competing, the route to MI phase is slightly kinetically favored below 18 GPa.

(iii) The densification pathways starting from QII are all mediated by high energy amorphous structures, indicating that the crystal-to-crystal transition must be accompanied by amorphization.

Acknowledgements

This work was supported by the National Science Foundation of China (21533001), the 973 program (2013CB834603), the Science and Technology Commission of Shanghai Municipality (08DZ2270500).

Notes and references

- 1 D. Machon, F. Meersman, M. C. Wilding, M. Wilson and P. F. McMillan, *Prog. Mater. Sci.*, 2014, **61**, 216–282.
- 2 T. Tuma, A. Pantazi, M. Le Gallo, A. Sebastian and E. Eleftheriou, *Nat. Nanotechnol.*, 2016, **11**, 693–699.
- 3 R. J. Hemley, A. P. Jephcoat, H. K. Mao, L. C. Ming and M. H. Manghnani, *Nature*, 1988, **334**, 52–54.
- 4 L. E. McNeil and M. Grimsditch, *Phys. Rev. Lett.*, 1992, **68**, 83–85.
- 5 C. Meade and R. Jeanloz, *Science*, 1991, **252**, 68–72.
- 6 K. J. Kingma, R. J. Hemley, H.-K. Mao and D. R. Veblen, *Phys. Rev. Lett.*, 1993, **70**, 3927–3930.
- 7 K. J. Kingma, H.-K. Mao and R. J. Hemley, *High Pressure Res.*, 1996, **14**, 363–374.
- 8 E. Gregoryanz, R. J. Hemley, H.-K. Mao and P. Gillet, *Phys. Rev. Lett.*, 2000, **84**, 3117–3120.
- 9 J. Haines, J. M. Léger, F. Gorelli and M. Hanfland, *Phys. Rev. Lett.*, 2001, **87**, 155503.
- 10 J. Zhang, B. Li, W. Utsumi and R. C. Liebermann, *Phys. Chem. Miner.*, 1996, **23**, 1–10.
- 11 Y. Tsuchida and T. Yagi, *Nature*, 1990, **347**, 267–269.
- 12 M. Wu, Y. Liang, J.-Z. Jiang and J. S. Tse, *Sci. Rep.*, 2012, **2**, 398.
- 13 M. S. Somayazulu, S. M. Sharma and S. K. Sikka, *Phys. Rev. Lett.*, 1994, **73**, 98–101.
- 14 R. M. Wentzcovitch, C. da Silva, J. R. Chelikowsky and N. Binggeli, *Phys. Rev. Lett.*, 1998, **80**, 2149–2152.
- 15 R. Martoňák, D. Donadio, A. R. Oganov and M. Parrinello, *Phys. Rev. B: Condens. Matter Mater. Phys.*, 2007, **76**, 014120.
- 16 C. Shang and Z.-P. Liu, *J. Chem. Theory Comput.*, 2013, **9**, 1838–1845.
- 17 X.-J. Zhang, C. Shang and Z.-P. Liu, *J. Chem. Theory Comput.*, 2013, **9**, 3252–3260.
- 18 C. Shang, X.-J. Zhang and Z.-P. Liu, *Phys. Chem. Chem. Phys.*, 2014, **16**, 17845–17856.
- 19 F. Wang and D. P. Landau, *Phys. Rev. Lett.*, 2001, **86**, 2050–2053.
- 20 C. Shang, W.-N. Zhao and Z.-P. Liu, *J. Phys.: Condens. Matter*, 2015, **27**, 134203.
- 21 X.-J. Zhang, C. Shang and Z.-P. Liu, *J. Chem. Theory Comput.*, 2013, **9**, 5745–5753.
- 22 K. J. Caspersen and E. A. Carter, *Proc. Natl. Acad. Sci. U. S. A.*, 2005, **102**, 6738–6743.
- 23 X.-J. Zhang and Z.-P. Liu, *Phys. Chem. Chem. Phys.*, 2015, **17**, 2757–2769.
- 24 X.-J. Zhang and Z.-P. Liu, *J. Chem. Theory Comput.*, 2015, **11**, 4885–4894.
- 25 S.-H. Guan, X.-J. Zhang and Z.-P. Liu, *J. Am. Chem. Soc.*, 2015, **137**, 8010–8013.
- 26 S.-C. Zhu, S.-H. Xie and Z.-P. Liu, *J. Am. Chem. Soc.*, 2015, **137**, 11532–11539.
- 27 D. J. Wales, *Mol. Phys.*, 2002, **100**, 3285–3305.
- 28 B. W. H. van Beest, G. J. Kramer and R. A. van Santen, *Phys. Rev. Lett.*, 1990, **64**, 1955–1958.
- 29 R. Martoňák, D. Donadio, A. R. Oganov and M. Parrinello, *Nat. Mater.*, 2006, **5**, 623–626.
- 30 I. Saika-Voivod, F. Sciortino, T. Grande and P. H. Poole, *Phys. Rev. E: Stat., Nonlinear, Soft Matter Phys.*, 2004, **70**, 061507.
- 31 G. Kresse and J. Hafner, *Phys. Rev. B: Condens. Matter Mater. Phys.*, 1993, **47**, 558–561.

- 32 G. Kresse and J. Furthmüller, *Comput. Mater. Sci.*, 1996, **6**, 15–50.
- 33 G. Kresse and D. Joubert, *Phys. Rev. B: Condens. Matter Mater. Phys.*, 1999, **59**, 1758–1775.
- 34 J. P. Perdew, K. Burke and M. Ernzerhof, *Phys. Rev. Lett.*, 1996, **77**, 3865–3868.
- 35 H. J. Monkhorst and J. D. Pack, *Phys. Rev. B: Condens. Matter Mater. Phys.*, 1976, **13**, 5188–5192.
- 36 M. S. José, A. Emilio, D. G. Julian, G. Alberto, J. Javier, O. Pablo and S.-P. Daniel, *J. Phys.: Condens. Matter*, 2002, **14**, 2745.
- 37 J. Junquera, Ó. Paz, D. Sánchez-Portal and E. Artacho, *Phys. Rev. B: Condens. Matter Mater. Phys.*, 2001, **64**, 235111.
- 38 N. Troullier and J. L. Martins, *Phys. Rev. B: Condens. Matter Mater. Phys.*, 1991, **43**, 1993–2006.
- 39 S. Nosé, *J. Chem. Phys.*, 1984, **81**, 511–519.
- 40 W. G. Hoover, *Phys. Rev. A: At., Mol., Opt. Phys.*, 1985, **31**, 1695–1697.
- 41 M. Parrinello and A. Rahman, *Phys. Rev. Lett.*, 1980, **45**, 1196–1199.
- 42 M. Akaogi, H. Yusa, K. Shiraishi and T. Suzuki, *J. Geophys. Res.: Solid Earth*, 1995, **100**, 22337–22347.
- 43 C. Lee and X. Gonze, *Phys. Rev. B: Condens. Matter Mater. Phys.*, 1995, **51**, 8610–8613.
- 44 P. J. Steinhardt, D. R. Nelson and M. Ronchetti, *Phys. Rev. B: Condens. Matter Mater. Phys.*, 1983, **28**, 784–805.
- 45 R. Palmeri, M. L. Frezzotti, G. Godard and R. J. Davies, *J. Metamorph. Geol.*, 2009, **27**, 685–705.
- 46 S.-H. Guan and Z.-P. Liu, *Phys. Chem. Chem. Phys.*, 2016, **18**, 4527–4534.
- 47 A. K. David and T. D. Martin, *J. Phys.: Condens. Matter*, 1999, **11**, 9263.
- 48 G. Malavasi, M. C. Menziani, A. Pedone, B. Civalleri, M. Corno and P. Ugliengo, *Theor. Chem. Acc.*, 2007, **117**, 933–942.